PAPER

Check for updates

Adsorptive removal of aflatoxin B₁ from water and edible oil by dopamine-grafted biomass chitosan–iron–cobalt spinel oxide nanocomposite: mechanism, kinetics, equilibrium, thermodynamics, and oil quality†

N. Abasi,[a] A. R. Faraji [ID] *[bc] and A. Davood[a]

Currently, the use of magnetic physical adsorbents for detoxification is widely applied in the food industry; however, the fabrication of high-efficiency low-cost absorbents without damaging the nutritional quality of food is a major challenge. Herein, a simple, green, efficient, and cost-effective method for the magnetic solid-phase extraction of aflatoxin B₁ (AFB₁) from edible oils and aqueous matrices was developed using a dopamine-loaded biomass chitosan–iron–cobalt spinel oxide nanocomposite (DC/CFOS NC). The characterization, physicochemical processes, mechanism, and reusability of DC/CFOS were systematically evaluated in detail. It was found that the adsorption characteristic of DC/CFOS NC was accurately represented by the pseudo-second-order kinetics ($k_2 = 0.199$ g mg⁻¹ min⁻¹) and Freundlich isotherm models ($K_f = 1.139$ (mg g⁻¹) (L mg⁻¹), $R^2 = 0.991$)), and its adsorptive process is feasible, spontaneous, and exothermic. Benefiting from its high specific surface area, microporous structure, and polar/non-polar active sites, the as-prepared DC/CFOS exhibited an excellent adsorption performance for AFB₁ (50.0 µg mL⁻¹), as measured using the Freundlich isotherm model. The mechanistic studies demonstrated that the synergistic effects of the surface complexation and electrostatic interactions between the functional groups of DC/CFOS NC and AFB₁ were the dominant adsorption pathways. Besides, DC/CFOS exhibited negligible impacts on the nutritional quality of the oil after the removal process and storage. Thus, DC/CFOS NC showed sufficient efficacy and safety in the removal of AFB₁ from contaminated edible oil.

1. Introduction

AFB₁ is a toxic, secondary metabolite produced by some Aspergillus species (*e.g.*, *A. flavus* and *A. parasiticus*), which can cause various complications, such as hepatotoxic, genotoxic, teratogenic, and immunotoxic impacts in animals and humans.[1,2] AFB₁ is recognized as a human group 1 carcinogen by the International Agency for Research on Cancer. Based on the European Union, the maximum permissible limits of 4.00 µg kg⁻¹ total aflatoxins and 8.00 µg kg⁻¹ AFB₁ have been considered in food exposed to sorting or physical treatment before human consumption, and the corresponding value of 2.0 µg kg⁻¹ AFB₁ for direct human consumption.[3] Alternatively, the U.S. Food and Drug Administration stipulates that the content of aflatoxins in human food cannot exceed 20 ng kg⁻¹. Therefore, the development of strategies that effectually reduce or eliminate AFB₁ contamination from food commodities holds practical importance for food safety and export trade. Recently, many technologies have been adopted to remove AFB₁, including chemical catalysis,[2] photocatalytic degradation,[4] biodegradation,[5] and adsorption.[6,7] Among these techniques, adsorption is introduced as a method with unique potential due to its high performance, ease and reliability of operation, low cost, strong operability, simultaneous removal of multiple pollution sources in one treatment process, and low toxicity.[8] Thereby, it is considered desirable to fabricate novel nano-adsorbents with specific structures and high adsorption performances that are highly selective and safe to apply and would not have a negative impact on the nutritional quality of food commodities.[1] Adsorption binders as a key component of the adsorption process have attracted significant attention, and consequently many inorganic (such as resins, mineral clay, attapulgite, bentonite, kaolinite, Fe/3D-WS₂ nanoflowers, and

[a]Department of Medicinal Chemistry, Faculty of Pharmaceutical Sciences, Tehran Medical Sciences, Islamic Azad University, Tehran, Iran

[b]Department of Organic Chemistry, Faculty of Pharmaceutical Chemistry, Tehran Medical Sciences, Islamic Azad University, Tehran, Iran. E-mail: a.faraji@iaups.ac.ir; alireza_ch57@yahoo.com; Fax: +98 21 22600099; Tel: +98 21 22640051

[c]Nutrition and Food Sciences Research Center, Tehran Medical Sciences, Islamic Azad University, Tehran, Iran

† Electronic supplementary information (ESI) available. See DOI: https://doi.org/10.1039/d3ra06495f

flower-like mesoporous magnesium silicate composites), organic (such as activated carbon, β-D-glucans, chitosan, cellulose, and plant derivatives), and biological (such as lactic acid bacteria, laccase-inorganic hybrid nanoflower, and yeast cell walls) adsorbents have been utilized.[9–16] Nonetheless, to realize the challenging adsorption in future industries, high-quality adsorbents are still required. An adsorbent can be bound to the target toxins mostly based on the differences in the hydrophilic and hydrophobic nature of the adsorbent, and consequently interaction between the adsorbent with the toxin and matrices.[8] Especially, organic phase adsorption is considered more challenging due to the affinity issues of many adsorbents to the polar AFB$_1$.

Chitosan, as the second most abundant naturally available polymer, is insoluble at neutral and high pH value, resulting in the poor adsorption of AFB$_1$ in aqueous solution. Furthermore, its low surface area, weak mechanical properties, and low porosity limit its use.[17] Alternatively, the adsorbed AFB$_1$ may be released to the environment after adsorption due to the weak interactions between them. According to these drawbacks, chitosan-based adsorbents need to be functionalized with hydrophilic/hydrophobic materials.[17]

To the best of our knowledge, no data have been reported on the utilization of nitrogen and carbon-enriched chitosan biomass as an adsorbent for the efficient treatment of AFB$_1$. Thus, we report the preparation of a porous magnetically recoverable dopamine/amino-functionalized cobalt ferrite from chitosan biomass nanoparticles (DC/CFOS NC) for the removal of AFB$_1$ from various matrices. Specifically, the excellent adsorptive activities of the porous DC/CFOS NCs are related to the unique properties of the supermagnetic cobalt ferrite particles, which act as a non-toxic, low-cost and durable magnetic carrier with environmental compatibility. The non-toxic and biocompatible silica act as a dispersing agent and compact coating without interfering with the inherent characteristic of the magnetic beads, preventing against oxidation and/or aggregation during the preparation stages. The three-dimensional chitosan biomass network acts as a porous organic polymer platform with many advantages such as abundant availability, low price, non-toxic nature, excellent biocompatibility, tunable surface properties, antibacterial activity and biodegradability. The carbon-enriched modification reduces the hydrophilicity and enhances the adsorptive affinity with AFB$_1$ in oil matrices, while the loaded dopamine/amine act as multi adsorptive active sites for effective binding to AFB$_1$, and also providing more accessible absorptive sites compared to the inner sites of chitosan frameworks. Alternatively, the acid-treated chitosan is slightly positively charged due to the protonation of oxygen/nitrogen, which causes repulsion between these positively charged particles by Coulomb interaction. Therefore, the aqueous solution of the chitosan nanoparticles became a colloidal suspension without the need for organic solvent or surfactant. Finally, this work can promote the utilization of DC/CFOS NC as a magnetically recoverable adsorbent for the effective detoxification of AFB$_1$ from two different polar conditions, i.e., organic phase and aqueous phase, and economical, feasible, and efficient strategy in the food industry.

2. Experimental

2.1. Chemicals

All materials including dopamine (4-(2-aminoethyl) benzene-1,2-diol, $C_8H_{11}NO_2$), medium molecular weight chitosan (CS, $C_{56}H_{103}N_9O_{39}$, >95%), tetraethyl orthosilicate (TEOS), oleic acid (OA), acetonitrile (CH_3CN, ACN), isopropyl alcohol (C_3H_8O, IPA), N-(2-aminoethyl)-3-aminopropyltrimethoxysilane (AEAPS), nitric acid (HNO_3), potassium iodide (KI, 99%), EtOH, NaOH, NH_3, $Fe(NO_3)_3 \cdot 9H_2O$, $Co(OAc)_2 \cdot 4H_2O$ and aflatoxin B_1 ((6aR,9aS)-4-methoxy-2,3,6a,9a tetrahydrocyclopenta[c]furo [3′,2′:4,5]furo[2,3-h][1]benzopyran-1,11-dione, $C_{17}H_{12}O_6$) were obtained from Merck and Sigma-Aldrich and used as received without further purification.

2.2. Synthesis of DC/CFOS NC

DC/CFOS NC was synthesized using modified co-precipitation and Stöber methods.[18] Stoichiometric quantities (2.0 : 1.0 mol mol^{-1}) of $Fe(NO_3)_3 \cdot 9H_2O$ (400 mg) and $Co(OAc)_2 \cdot 4H_2O$ (200 mg) were homogenized in 20 mL deionized water under an N$_2$ atmosphere. Then, the solution was slowly poured into a well-stirred NaOH solution at 75 °C for 30 min. After the addition of NaOH, a color change was observed from light blue to yellow. Under continuous stirring, 25.0 mg OA was added dropwise to the system. The obtained dark-brown cobalt ferrite nanoparticles (CFO NPs) were washed three times with distilled water and three times with EtOH, and then dried on a stove at 60 °C. Then, 5.0 g of chitosan was incubated for 30 min at a high temperature and gradually added to 30 mL dilute acid nitric (2.0% v/v) solution under mechanical stirring. Afterward, the obtained solid was washed four times with distilled water (DW) and dried in a vacuum oven at 90 °C to neutralize the protonated chitosan NPs (CS$^+$). The CFOS NPs were obtained by reacting the neutralized CFO NPs with TEOS through the co-participation method. In another balloon, 0.15 g of $CoFe_2O_4$–SiO_2 (CFOS) and 1.0 mL AEAPS were dispersed in 40 mL of IPA under reflux for 6.0 h. Subsequently, $CoFe_2O_4$–SiO_2-AEAPS (CFOS-NH$_2$) was purified several times using IPA (2 × 4 mL) and DW (3 × 5 mL). To prove the successful preparation of CFOS-NH$_2$, the Ninhydrin test was performed. To synthesize the magnetic chitosan/CFOS-NH$_2$ (C/CFOS), NH$_3$ (50 mL 30%, v/v) and NaOH (40.0 mL) were gently added to a suspension of CFOS-NH$_2$ (4.0 g) and chitosan NPs (4.0 g) under an N$_2$ atmosphere at 80 °C for 2.0 h. At the end of this stage, the reaction temperature was increased to 90 °C and the mixture stirred for 1.0 h. After cooling to room temperature, the deep-brown solid was washed with DW twice and absolute EtOH once, neutralized, and dried in a vacuum oven at 60 °C for 3.0 h. Finally, C/CFOS (0.2 g) dopamine (1.0 g), NaOH (20 mL, 1.0 mM), and KI (10.0 mg) were added to 50 mL of ACN and stirred at room temperature and 600 rpm for 5.0 h. Then, the resulting product was magnetically separated, washed several times with DW and absolute EtOH/ACN, and then dried in a vacuum oven at 60–70 °C. Detailed information on the synthesis of the adsorbent and its characterization tools is described in Fig. 1S and Text 1S in the ESI.†

Finally, to measure the percentage of grafted dopamine in DC/CFOS NCs, thermogravimetric analysis was conducted at a constant rate of 10 °C min⁻¹ to 800 °C min⁻¹ under an N₂ atmosphere (20 mL min⁻¹). The weight loss at 30–200 °C was due to the elimination of H₂O adsorbed by the surface or cavity of DC/CFOS NPs, while that at 200–700 °C was related to the depolymerization of the chitosan units, dopamine moieties, and metal oxides. Based on the weight loss, the GD (percentage of grafted dopamine) was calculated using eqn (1), as follows:

$$GD = \frac{M_1 - M_2}{M_0} \times 100 \tag{1}$$

where GD is grafted dopamine (%), M_1 is the mass loss of DC/CFOS NC at 30–800 °C (mg), M_2 is the mass loss of DC/CFOS NC at 30–200 °C, and M_0 is mass of DC/CFOS NC (mg) (Fig. 1).

2.3. Batch adsorption experiments

2.3.1. Optimization experiment. The detailed information on the safety precautions is explained in Text 2S and Table 1S.† Initially, a primary stock solution of AFB₁ was prepared in ACN, which was then diluted to 50.0 μg mL⁻¹ using DW. The adsorption tests were performed in 10 mL-capacity flasks, and 1.0 mL of AFB₁ spiked solution was added to the working reactor with 2.5 mg of DC/CFOS NCs. The flask was protected with aluminum foil from shaking and light until adsorption equilibrium was reached. After a certain time, the magnetic adsorbent was isolated by an external magnet, and then HPLC and UV-Vis were utilized to detect the supernatant AFB₁. The adsorption capacity and removal efficiency of AFB₁ over DC/CFOS NC in water and edible vegetable oil samples were measured using eqn (2)–(4).

$$D_{ads} = \frac{C_0 - C_t}{C_0} \times 100 \tag{2}$$

$$Q_t = \frac{C_0 - C_t}{M} \times V \tag{3}$$

$$Q_e = \frac{C_0 - C_e}{M} \times V \tag{4}$$

where D_{ads} is adsorptive detoxification efficiency (%), Q_t is adsorption capacity at a specific time (mg g⁻¹), Q_e is the adsorption capacity at equilibrium (mg g⁻¹), C_t is the concentration of AFB₁ at the intended time (mg L⁻¹), C_e is the concentration of AFB₁ at equilibrium (mg L⁻¹), M is the DC/CFOS NC dosage (g), and V is the sample volume (L). Subsequently, multiple group adsorption experiments were conducted to assess the impact on the removal of AFB₁ from aqueous solution by varying: 50 < [AFB₁]₀ < 150 μg mL⁻¹, 0.5 < [DC/CFOS]₀ < 3.5 mg, 3.0 < pH < 9.0, and 10 < contact time <120 min.

2.3.2. Adsorption isotherm models. The description of the interactive behavior between the different initial dosages of AFB₁ (50–100 μg mL⁻¹) and DC/CFOS NC at four temperatures (278, 288, 298 and 308 K) and the evaluation of the adsorptive capacities of DC/CFOS NC were investigated using the Langmuir, Freundlich, Temkin isotherm, and Dubinin–Radushkevich adsorption isotherm models (eqn (5)–(9)).[10,11] Based on the value of the adsorption index (n) (eqn (6)), $n > 1$ or $n < 1$ indicates that the adsorption process is easy or difficult to occur, respectively. Besides, the separation factor (R_L) values demonstrate if the adsorption is unfavorable $(R_L > 1)$, linear $(R_L = 1)$, favorable $(0 < R_L < 1)$, and irreversible when $R_L = 0$ (eqn (7)).

$$\frac{C_e}{Q_e} = \frac{1}{Q_{max} K_L} + \frac{C_e}{Q_{max}} \tag{5}$$

$$\ln Q_e = \left(\frac{1}{n}\right) \ln C_e + \ln K_F \tag{6}$$

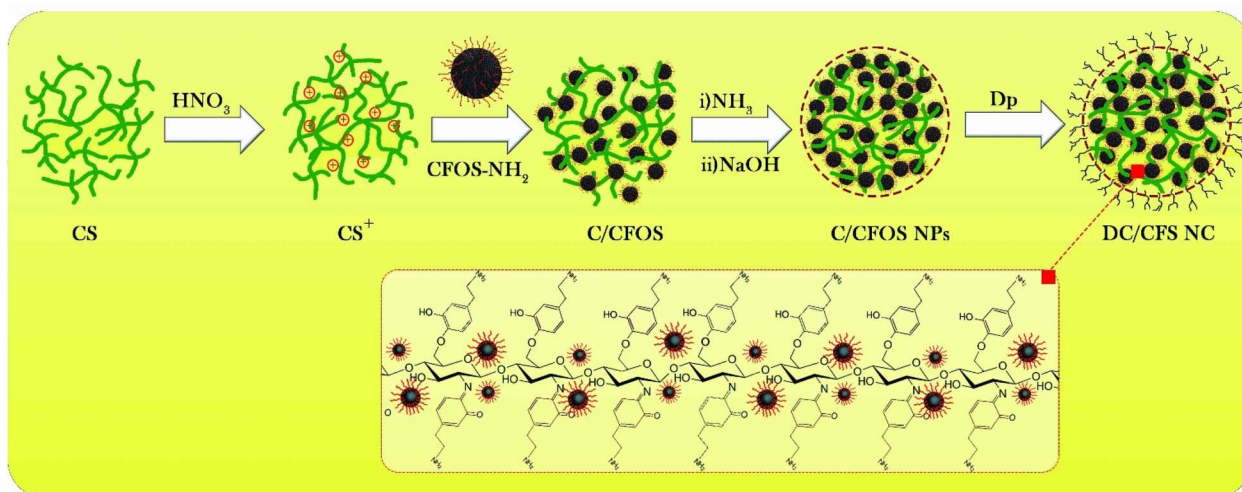$$R_L = \frac{1}{1 + K_L C_0} \tag{7}$$

$$Q_e = BT \ln K_T + BT \ln C_e \tag{8}$$

Fig. 1 Schematic illustration of the synthesis of DC/CFOS.

$$Q_e = Q_m \exp^{\beta\left[RT \ln\left(1+\frac{1}{C_e}\right)\right]^2} \tag{9}$$

where Q_e is the adsorption capacity at equilibrium (mg g^{-1}), Q_{max} is the maximum adsorption capacity (mg g^{-1}), C_e is the concentration of AFB$_1$ at equilibrium (mg L^{-1}), C_0 is the initial concentration of AFB$_1$ (mg L^{-1}), K_L is the Langmuir constant (L mg^{-1}), K_F is the Freundlich constant ((mg g^{-1}) (L mg^{-1})$^{1/n}$), n is the adsorption index, R_L is the separation factor (mg g^{-1}) (L mg^{-1})$^{1/n}$), K_T is the Temkin constant (L mg^{-1}), T is temperature (K), B and R are the universal gas constant (J mol^{-1} K^{-1}) and β is a constant related to the adsorption energy.

2.3.3. AFB1 adsorption kinetic study. The kinetics for the adsorption of 50.0 µg mL^{-1} AFB$_1$ on DC/CFOS NC was investigated using the quasi-1st-order and quasi-2nd-order kinetic models in a constant-temperature laboratory (25 °C) at various times (0.5, 1.0, 1.5, 2.0, and 2.5 h) (eqn (10) and (11)), respectively.[6,11,13]

$$Q_t = Q_e - Q_e e^{k_1 t} \tag{10}$$

$$Q_t = \frac{K_2 Q_e^2 t}{1 + K_2 + Q_e t} \tag{11}$$

where Q_t is the adsorption capacity at the intended time (mg g^{-1}), Q_e is the adsorption capacity at equilibrium (mg g^{-1}), t is the adsorption time (min), K_1 is the first-order constant rate (min^{-1}), and K_2 is the second-order constant rate (min^{-1}).

2.3.4. Adsorption thermodynamics study. To determine the temperature dependence, feasibility, spontaneity, and nature of the adsorption process, the values of the thermodynamic factors (*e.g.*, Gibbs free energy change (ΔG^0), standard entropy change (ΔS^0), and enthalpy change (ΔH^0)) were measured using the Van't Hoff equations (eqn (12)–(15)). The plot of ln(K_d) *vs.* $1/T$ was fitted to a straight line that has an intercept ($\Delta S^0/R$) and slope ($\Delta H^0/R$).

$$\Delta G^0 = \Delta H^0 - T \Delta S^0 \tag{12}$$

$$\Delta G^0 = RT \ln(K_d) \tag{13}$$

$$\ln K_d = -\frac{\Delta H^0}{RT} + \frac{\Delta S^0}{R} \tag{14}$$

$$K_d = \frac{Q_e}{C_e} \tag{15}$$

where K_d is the distribution coefficient (L mol^{-1}), ΔG^0 is the Gibbs free energy change (kJ mol^{-1}), ΔS^0 is the standard entropy change (J mol^{-1} K^{-1}), ΔH^0 is the enthalpy change (kJ mol^{-1}), R is the universal gas constant (J mol^{-1} K^{-1}), T is the temperature (K), Q_e is the adsorption capacity at equilibrium (mg g^{-1}), and C_e is the concentration of AFB$_1$ at equilibrium (mg L^{-1}).

2.3.5. Evaluation of the physicochemical qualities of edible oil after removal/storage process. 5.0 g contaminated edible oil sample containing 10.0 µg mL^{-1} of AFB$_1$ was treated by DC/CFOS NC. Then, a desired amount of treated oil was isolated from the removal system and stored for various times (0–180 days) at ambient temperature (25–27 °C). The important quality factors (*e.g.*, Ac (acidity), AV (acid value, mg g^{-1}), IV (iodine value, g. 100 g^{-1}), POV (peroxide value, g. 100 g^{-1}), p-AV (*p*-anisidine value), MV (moisture and volatile matters), D (refractive index), FFA (free fatty acid composition (*i.e.*, saturated fatty acids (SFAs) and unsaturated fatty acids (UFAs)) of the fresh and treated samples were measured to evaluate the influence of the catalytic removal system on the storage stability and quality characteristics of edible oil.

2.3.6. Desorption and regeneration studies. To assess the durability and reusability of DC/CFOS NC, recoverability tests were performed in several adsorption–desorption runs. Briefly, DC/CFOS NC was magnetically separated, and then immersed in 15 mL ACN : DW (87 : 13, v/v) under mechanical stirring for 50 min. Afterward, the used DC/CFOS NC was purified several times by DW (4 × 5 mL) and CH$_3$CN (2 × 5 mL), respectively, and reused in the next run. The Q_e and D_{ads} of AFB$_1$ were determined after each run to evaluate the durability/ recyclability of DC/CFOS NC.

3. Results and discussion

3.1. Characterization

Fig. 2 displays the SEM/HRTEM images of the as-prepared DC/ CFOS NC. The HRTEM and SEM images of DC/CFOS NC indicate that it is visible and dominantly composed of quasi-spherical NPs with a size of *ca.* 26 nm. The high-resolution TEM images of DC/CFOS NC show the presence of distinct irregular crystals of CFOS spread throughout the amorphous phase and the rough and porous surface texture of the chitosan–dopamine template. Besides, it can be found that CFOS NPs were well dispersed due to the intimate interaction between CFOS-AEAPS NPs and chitosan. These strong interactions limit the agglomeration of the crystalline DC/CFOS to some extent. Also, different degrees of deformed lattices can be seen in the HRTEM images, demonstrating the existence of intrinsic defects in DC/CFOS NC. The streaks with a lattice spacing of 0.1881 nm can be related to the peak at the 2θ value of 35.55° in the XRD pattern. Indeed, the CS$^+$, oleic acid, and porous silica caused the favorable dispersion and segregation of the particles, and subsequently effectively impeded the fast growth of bimetallic grains during the fabrication of the adsorbent, and thus DC/CFOS displayed a small and relatively irregular size. As shown in the SEM images, DC/CFOS NC possessed a rough surface with several non-uniformly dispersed white spots on the chitosan scaffold, which can provide an active interface and diffusion channels for the toxin molecules. The elemental distribution of the adsorbent was determined by FESEM and EDS mapping (Fig. 2B), which illustrate the existence of Co, Fe, Si, C, O, and N in DC/CFOS NC. Besides, the average particle size is 24.5 ± 08.4 nm with a rather narrow distribution according to the DLS analysis, with most of the particles possessing a diameter of 10–80 nm (Fig. 2S†). Fig. 2G displays the different lattice fringes related to the inter-planar distance of the (1 1 1), (2 2 0), and (4 4 0) lattice planes. The resultant SAED pattern clearly shows the crystalline nature of the CFO NPs. The well-resolved interference lattice planes shown in the SAED images were also similar to the XRD results.
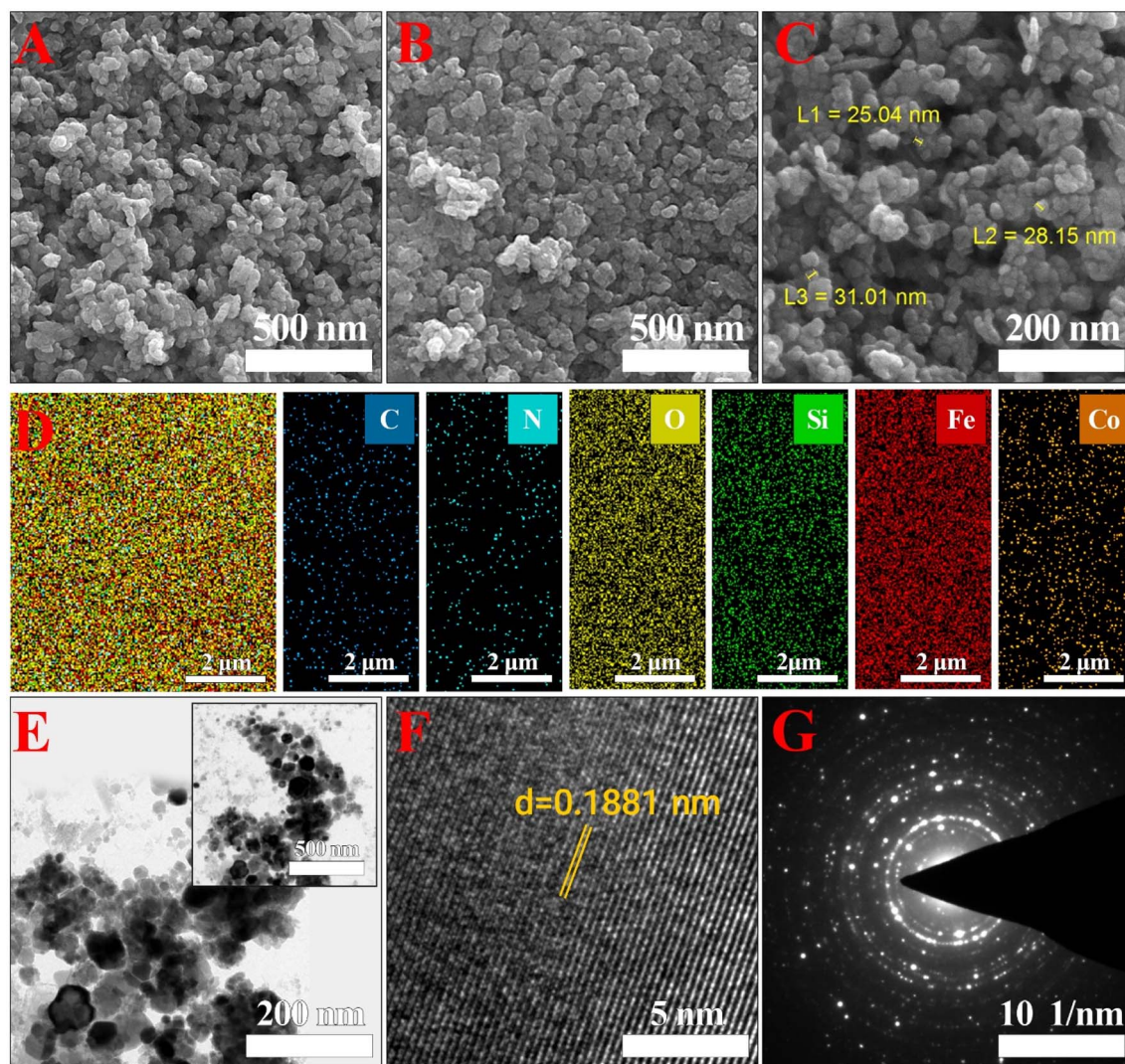
Fig. 2 Morphology and structure of DC/CFOS NC. (A–C) Representative SEM image, (D) FE-SEM, (E and F) HR-TEM images, and (G) SAED pattern of synthesized nanomaterial.

Fig. 3A exhibits the wide-angle XRD pattern of the CFO NP and DC/CFOS NC in the 2θ range of 10° and 70°. The relatively strong diffraction peaks located at 18.23°, 30.14°, 35.55°, 38.60°, 43.12°, 53.73°, 57.07° and 62.63° are indexed to the (1 1 1), (2 2 0), (3 1 1), (2 2 2), (4 0 0), (4 2 2), (5 1 1) and (4 4 0) planes of face center cubic of CFO NPs, respectively (JCPDS File No. 04-016-3954).[19] The weak characteristic crystalline peaks of chitosan at 2θ values of 12.4° and 20.3° were not observed in the XRD pattern of DC/CFSO. This can be attributed to the weaker intensity of these peak compared to the diffraction peak of CFO and good distribution of nano CS chains on CFSO-NH$_2$.[20] Besides, CS NPs are comprised of a compressed network structure of interpenetrating polymer chains cross-linked to CFSO-NH$_2$ and each other. Thus, the XRD results indicated a greater disarray in chain alignment in the CS NPs after grafting and cross-linking.[21] Furthermore, impurity peaks were not detected in the XRD pattern of DC/CFOS prepared herein, proving that it was comprised of high-purity CFO NPs. In the

XRD curve of DC/CFOS NC, the peak position and shape were relatively similar to that of CFO NPs. Alternatively, the broader peaks in the XRD curve of DS/CFOS NC indicated the lower crystallinity of DS/CFOS NC compared to the original CFOS NPs. These results confirm that the as-prepared DC/CFOS NC exhibited good crystallinity and the crystal structure of CFO NPs remained intact after their modification. The lack of significant change may be related to the presence of a protective and tight shell during the modification process.[22] Besides, the average grain sizes of the samples were measured using the Debye–Scherrer formula,[23] which indicated that CFO and DC/CFOS NC possessed grain sizes of about 8.50 and 11.1 nm, respectively. Additionally, to obtain the crystallinity of the samples on a quantitative basis, the CI value was determined using eqn (16), as follows

$$CI = \frac{(\text{Size of the sample by TEM or SEM})(\beta \cos \theta)}{k\ (\lambda)} \quad (16)$$
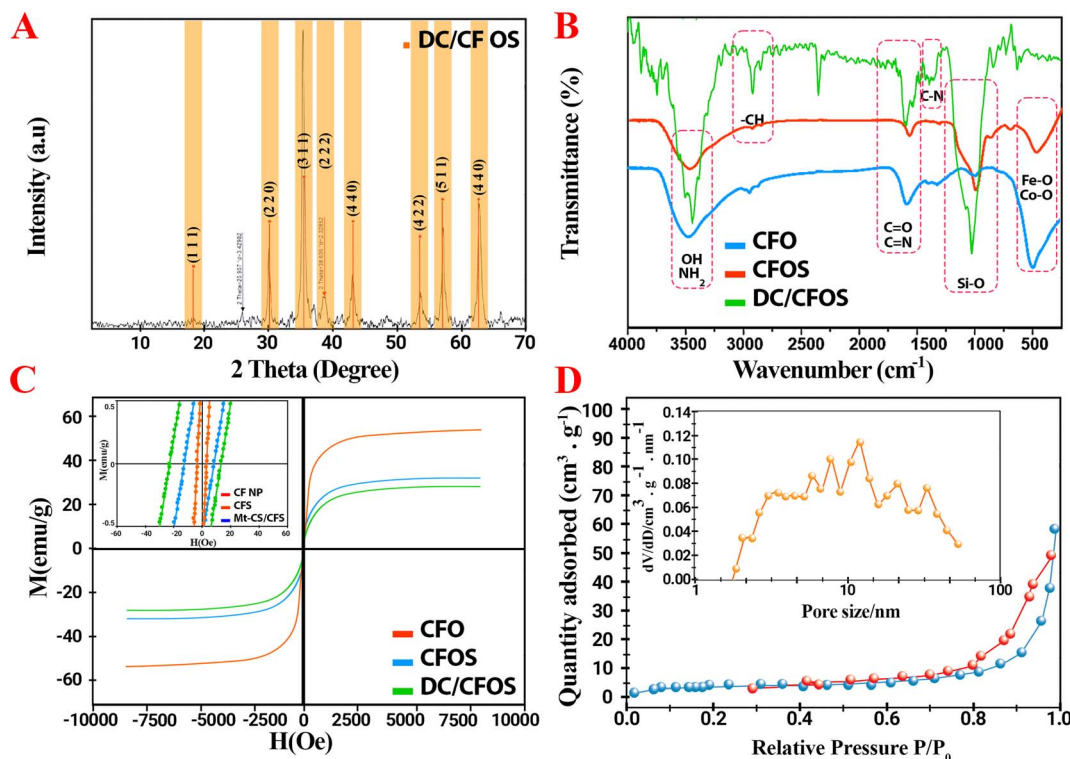
Fig. 3 Characterization of synthesized nanomaterial samples. (A) XRD pattern of DC/CFOS NC, (B) FT-IR spectra of CFO, CFOS, and DC/CFOS, (C) magnetic hysteresis curves of CFO, CFOS, and DC/CFOS [inset: low magnetic field], and (D) N$_2$ adsorption–desorption isotherms and BJH pore size distribution of DC/CFOS NC.

where β, θ, k, and λ are the line broadening at half the maximum intensity (FWHM), Bragg's angle, dimensionless shape factor, and X-ray wavelength, respectively. The data manifested that the CI of the same volume of CFSO and DC/CFOS NC was 2.0, and 2.17, respectively. Given that the high crystallinity index value is coupled with a low crystallite size, it can be concluded that DC/CFOS NC had a lower crystallinity compared to hercynite.

Fig. 3B exhibits the FTIR spectra of CFO and DC/CFOS NC in the range of 400 to 4000 cm^{-1}. The adsorption peaks observed at 429–443 cm^{-1}, $\sim$581–584 cm^{-1}, and 1110–1180 cm^{-1} correspond to the Fe–O, Co–O, and O–Si–O/Si–O–Si bonds in CFOS NPs, respectively.[24] In this investigation, OA was added to enhance the dispersibility of the CFOS particles; thereby, weak peaks appeared at 1628.3 and 1381.7 cm^{-1} in the FTIR spectrum of CFO related to the C=O and C–H groups of OA. In the FTIR spectrum of DC/CFOS NPs, the bands located at 3280–3445, 2921.36, 1568, 1435.8, and 1075.86 correspond to –OH (and surface-adsorbed O–H of water), –CH stretching, –NH stretching, –C–H bending, and C–O–C stretching, respectively. In addition, the characteristic peaks of DC/CFOS NC located at 1570–1631 cm^{-1} correspond to the aromatic-ring structure of dopamine and the C=N groups.[24,25] Thus, these results demonstrate that DC/CFOS NC was successfully synthesized.

To evaluate the magnetic field dependence of magnetization of CFO NP and DC/CFOS NC at room temperature, VSM was applied to measure the hysteresis curves of the materials. The

M_s (magnetic saturation) of the samples followed the order of CFO-OA/SiO$_2$ > CFO-SiO$_2$ >> DC/CFOS. The M_s of CFO-SiO$_2$ was 82.8% that of CFO-OA-SiO$_2$ due to the higher particle size and spin disorder on the surface of the bulk CFO-SiO$_2$.[26] As shown in Fig. 3C, with an enhancement in the magnetic field strength, the magnetization of CFO NPs and DC/CFOS increased. According to these graphics, both the CFO NPs and DC/CFOS NC exhibit magnetic behavior with a very low coercive field ($\sim$14–16 Oe) and M_s/M_r ratio (0.06–0.07) compared to that in other studies due to their multi-domain structure and facile movement of their domain walls.[25] To further clarify this, the critical size of a mono-domain particle (D_m) was calculated using eqn (17).

$$D_m = 9 \times (2K_B T_C |K_1|/a)^{1/2}/(6.28\ M_s^2) \quad (17)$$

where $|K_1|$ is the magneto-crystalline anisotropy constant (3.80 × 10^6 erg cm^{-3}), T_C is the Curie temperature (677 K), M_s is the saturation magnetization (310 Gs), K_B is the Boltzmann constant (1.3806452 × 10^{-23} J K^{-1}), and a is the lattice constant (8.385 × 10^{-8} cm).

Given that the particle size (28.0 nm) is much smaller than D_m (428 nm), the particles exist in a mono-domain structure. Indeed, when the particle size and coercive field decreased, the magnetic nature of DC/CFOS gradually transformed from a ferromagnetic to superparamagnetic state. The M_s value of DC/CFOS NC decreased to 28.10 emu g^{-1} compared to the

original CFO NPs (58.12 emu g^{-1}) due to the non-magnetic dopamine/chitosan/silica covering on CFO. Besides, the M_r value determined in DC/CFOS NC varied between 0.61 to 1.33 emu g^{-1}, proving that the morphological shape of the particles was quasi-spherical. The inset picture in Fig. 3C shows the macroscopic performance of the adsorbent, in which DC/CFOS NC could be rapidly dispersed in the aqueous medium, affording a homogeneous suspension. Also, DC/CFOS NC rapidly (<45 s) aggregated on the container wall when an external magnet field was introduced. Thereby, the as-prepared DC/CFOS has the supermagnetic characteristic and can act as a magnetically recoverable adsorbent.

The micro-structure of DC/CFOS NC and the precursor samples was measured by adsorption–desorption, as exhibited in Fig. 3D. Consistent with the IUPAC classification, the samples show a IV type isotherm with a hysteresis loop, corresponding to mesoporous structures.[23,27] Thus, it can be concluded that the introduction of a multi-layer shell resulted in a remarkable enhancement in specific surface area (S_{BET}) and median pore diameter (MPD). According to the data shown in Fig. 3D and using the BET equation, the S_{BET} and MPD of CFO NPs and DC/CFOS NC determined to be 11.20 m^2 g^{-1} and 23.22 m^2 g^{-1} and 5.35 nm and 15.45 nm, respectively. According to the BET results, DC/CFOS NC had a larger S_{BET} and MPD compared to the precursor sample. In the case of DC/CFOS NC, the empty pores were perceived by N$_2$ adsorption during the pore size distribution measurements, which confirmed that AFB$_1$ can fill the pores inside DC/CFOS NC. Thus, the highly porous nature of the as-prepared DC/CFOS NC with a large specific surface area facilitates the contact between the toxin and adsorbent, thereby accelerating the detoxification of AFB$_1$ from water and oil matrices.

Fig. 4A and B exhibit the TG/DTG curves of the original CFO NPs and fabricated DC/CFOS NC. There are three thermal stages of degradation in the TG/DTG curves of DC/CFOS. The initial peak appeared at ∼25–110 °C, which is related to the loss of humidity and absorbed water/solvent in the inner polymer, corresponding to about 4.87% weight loss.[28] The major weight loss began at ∼264.7 °C for DC/CFOS NCs and reached the maximum of ∼338.3 °C. The third peak (341–523 °C) is also a rapid degradation process, where in this step, ∼31.2% weight

loss occurred due to the decomposition of the polymer moiety in DC/CFOS NC. Thus, DC/CFOS NC has thermal durability for the adsorptive process, which is mainly due to the favorable cross-linking between the polymeric multi-layer components.

Besides, the electronegativity on the surface, changes in the surface charge upon adsorption, and colloidal stability were evaluated by ζ-potential studies (Fig. 3S†). In general, the numerical magnitude of the ζ-potential reflects the size and type of charges on the surface of compounds. As can be seen, the magnitude of the ζ-potential of −28.4 mV for DC/CFOS indicates the enhanced stability of the colloidal solution compared to the original CFO NPs (−18.40 mV). Additionally, the ζ-potential values of DC/CFOS demonstrate that it contains positively charged groups at pH < 6.73, which may be related to the formation of –NH$_3^+$ and –OH$_2^+$ under acidic conditions in the DC/CFO electrolyte solution. Thus, due to the high ζ-potential, the electrolyte solution was slightly affected by the change in the pH of the solution. At pH > 6.73, the ζ-potentials were negative, indicating the coexistence of –NH$_3^+$, –C=NH$^+$–, –NH$_2$OH$^-$, and C=NHOH$^-$ and demonstrating strong ability to combine with AFB$_1$ *via* electrostatic attraction under neutral conditions.

3.2. Ninhydrin test

The FT-IR results did not give proof of the existence of an amine group in CFOS-NH$_2$. Thus, it was detected based on the 'ninhydrin test', in which two molecules of ninhydrin (2,2-dihydroxyindane-1,3-dione) as an oxidizing agent react with one CFOS-NH$_2$ molecule to form Ruhemann's purple. Indeed, 2.0 mg L^{-1} of ninhydrin causes the release of amine *via* the concomitant condensation between 2-amino-1,3-indanedione and a second molecule of NINH. In this case, CFOS-NH$_2$ was placed in a water bath at 80 °C for 15 min. After cooling and isolation of the gathered magnetic solid, Ruhemann's purple chromophore was formed, thus illustrating the superficial amination of the magnetic core–shell composite (Fig. 5).

3.3. Batch adsorption analysis

The adsorption performance of DC/CFOS NC is affected by the pH value, DC/CFOS concentration, dose of AFB$_1$, adsorption temperature, contact time, existence of additives (such as
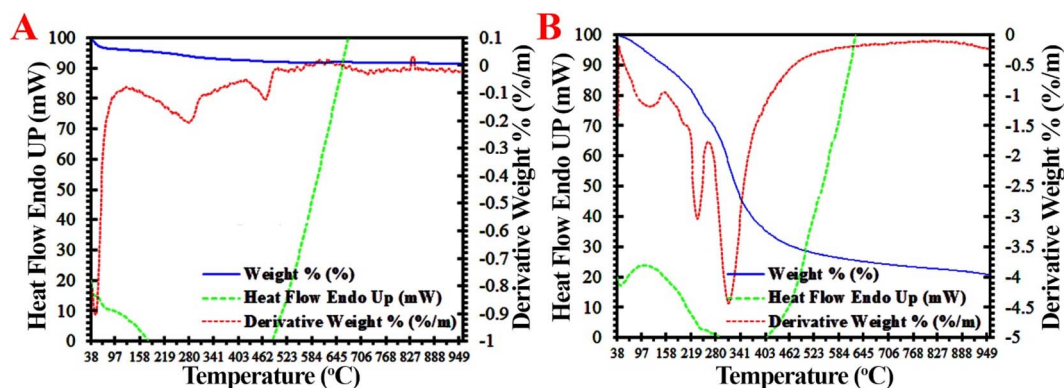

Fig. 4 Thermal gravimetric analysis of (A) CFO NPs and (B) DC/CFOS. The blue, red, and green lines are TGA, DTA, and heat flow endo up of as-prepared samples, respectively.
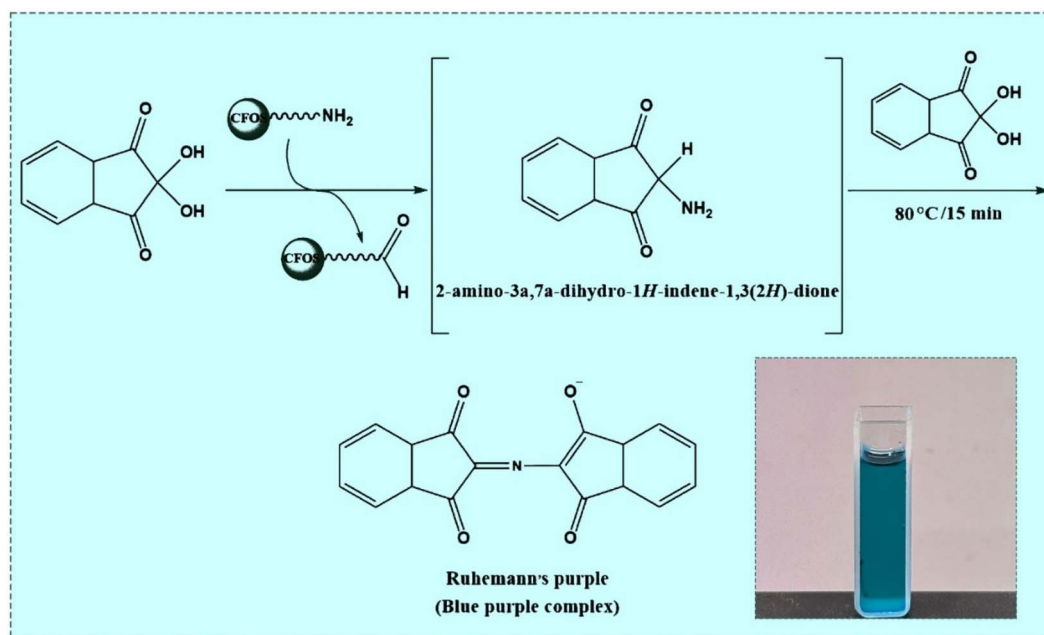
Fig. 5 Reaction of ninhydrin and H$_2$N-CFOS.

saturated/unsaturated organic acids and feed composition), and recoverability, and thus the stability of the DC/CFOS-AFB$_1$ bond is a vital parameter.

3.3.1. The effect of DC/CFOS NC concentration on AFB$_1$ removal. The effect of the concentration of DC/CFOS NC on the AFB$_1$ adsorption performance on DC/CFOS NC was investigated with a DC/CFOS NC concentration in the range of 0.5 mg L^{-1} to 3.5 mg L^{-1}, while keeping the initial dosage of AFB$_1$, contact time, and pH value of the solution fixed at 50 µg mL^{-1}, 100 min, and 7.0, respectively. It was found that the safety limit requirement was not achieved when the DC/CFOS NC concentration was low (<0.5 mg L^{-1}). The results showed that the AFB$_1$ removal efficiency gradually increased from 42.50% to 97.40% with an increasing amount of DC/CFOS NC from 0.50 to 2.50 mg L^{-1}, which may be because of the increase in the number of adsorptive sites. Additionally, the removal efficiency of 2.50 mg L^{-1} DC/CFOS NC was slightly higher than 3.50 mg L^{-1} DC/CFOS NC (Fig. 6A), which is due to the agglomeration of DC/CFOS NC at a higher concentration, causing diminished detoxification ability in water. Thus, the experimental results confirmed that the concentration of DC/CFOS NC of 2.5 mg L^{-1} is efficient to remove up to 97.40%
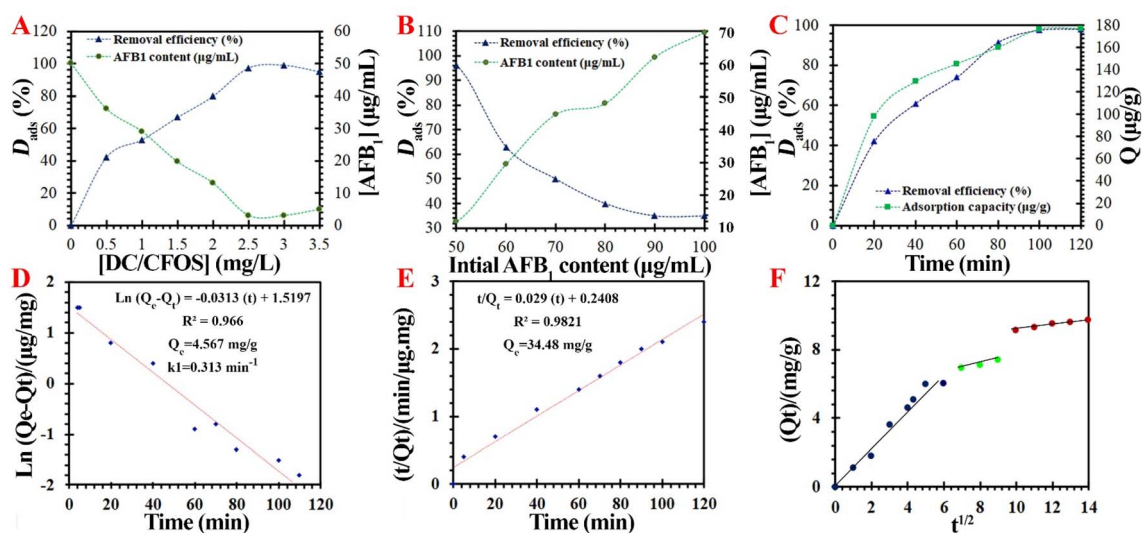

Fig. 6 Influence of different conditions on adsorption. (A) Adsorbent dosage, (B) initial AFB$_1$ concentration, (C) adsorption capacity/removal rate of adsorption AFB$_1$ at various times at pH 7.0, and fitting lines of (D) quasi-1st-order kinetic model, (E) quasi-2nd-order kinetic model, and (F) Weber–Moris intra-particle diffusion model.

AFB$_1$. Subsequently, 2.50 mg L^{-1} DC/CFOS NC was employed as the optimum concentration for further experiments due to the adsorption performance and running cost.

3.3.2. The effect of initial AFB$_1$ content on removal performance. The impact of the initial AFB$_1$ content (50, 60, 70, 80, 90, and 100 μg mL^{-1}) on the AFB$_1$ adsorption process was evaluated by performing the experiments with a varying toxin content for 120 min with a fixed solution of 2.5 mg L^{-1} DC/CFOS NC and pH value of 7.0. The adsorption efficiency is shown in Fig. 6B, where a higher AFB$_1$ dosage (>50.0 μg mL^{-1}) resulted in the lower removal efficiency of AFB$_1$ by DC/CFOS NC. Upon enhancing the initial AFB$_1$ content, the opportunity for AFB$_1$ to contact DC/CFOS NC was also enhanced. The removal percentage of AFB$_1$ declined with an increase in the initial AFB$_1$ concentration (>50.0 μg mL^{-1}) due to the saturation of the active adsorption sites in DC/CFOS NC, thus resulting in a decrease in the removal efficiency.

3.3.3. The effect of pH solution on removal AFB$_1$. The initial pH solution significantly changes the surface characteristics of substances (e.g., surface charge, acidity and basicity, and chemical/physical interactions).[29] Briefly, 0.06 mg of DC/CFOS NC was weighed and mixed with the 10.0 mL AFB$_1$ stock solution (100 μg mL^{-1}) and DW (20.0 mL) to achieve an AFB$_1$ dosage of 50.0 μg mL^{-1}, the pH value was adjusted to 3.0, 5.0, 7.0 or 9.0, and subsequently the UV absorption of the untreated and treated solutions was recorded using a UV-visible spectrophotometer at λ_{max} = 364 nm. At pH < pH$_{pzc}$, the surface of the adsorbent will be positively charged, which makes it easy to adsorb materials with a negative charge and vice versa. Thereby, at pH < 4.20, the surface of both AFB$_1$ and DC/CFOS NC (pH$_{pzc}$ = 6.73) was positively charged, which produced electrostatic repulsion between them. The D_{ads} (%) at pH 3.0, 4.0, 5.0, 6.0, and 7.0 was 83.20%, 84.10%, 89.50%, ~91.10%, and 97.40%, respectively. The experimental results demonstrated that the adsorption efficiency slightly improved with an increase in pH (4.20–6.73) due to electrostatic attraction. For more clarity, an acid immersion test was carried out.[13] Briefly, 5.0 mg of DC/CFOS NC was immersed in HCl solution with a pH value of 3.0 for 4.0 h, and then washed with EtOH and dried. The comparison of the FT-IR and N$_2$-adsorption–desorption data of the untreated DC/CFOS NC and acid-treated DC/CFOS NC illustrated that there is a difference in absorption intensity in some areas (Fig. 4S†). After the acid immersion, the intensity of the peaks at ~3570 cm^{-1} and 1645 cm^{-1}, which corresponded to the vibration of –OH, –NH$_2$, and C=O, decreased, respectively. Also, the difference between the N$_2$ adsorption–desorption isotherms and pore size distribution of the acid-treated DC/CFOS NC and DC/CFOS NC exhibited a slight change in MPD (14.20 nm) and S_{BET} (21.45 m^2 g^{-1}) after acid immersion due to the formation of $^+$H-DC/CFOS NC. The acid-treated DC/CFOS NC still had an adsorption capacity of 2.879 mg g^{-1} (D_{ads} = 80.12%) despite the blockage of its adsorptive centers (especially –OH and –NH$_2$) and capillary pores. Thus, the above-mentioned experimental results demonstrate that the specific interactions including polar/non-polar interactions (such as H-bonding, π–π, n–π, and hydrophobic interactions) play a more important role than pore

structure in the competitive AFB$_1$ adsorption. Here, given that the main method applied to improve the adsorption capacity was material loading modification (i.e., dopamine and IPA), some physicochemical properties and the adsorption capacity of the unmodified sample (C/CFOS) and chemically modified sample (DC/CFOS) were compared. The MPD and S_{BET} of DC/CFOS were 15.45 nm and 23.22 m^2 g^{-1}, which are slightly higher than that of C/CFOS (Table 1). Alternatively, the unmodified C/CFOS was significantly less efficient (D_{ads} = ~53.50%) than the chemically modified DC/CFOS (D_{ads} = 93.10%). Thus, dopamine/IPA modification of C/CFOS enhanced its MPD, and S_{BET} and absorption efficiency for AFB$_1$. Thereby, the chemical composition of DC/CFOS plays a more important role than its pore structure.

3.3.4. Adsorption kinetics. To further evaluate the mechanism for the adsorption of AFB$_1$ by DC/CFOS NC at room temperature and pH 7.0, various kinetic models were applied to assess the experimental data. The quasi-1st-order, quasi-2nd-order, and inter-particle kinetic rate models were applied to comprehend the adsorption process, and the corresponding factors and the linear regression coefficient value (R^2) are summarized in Table 2. The results indicated that the quasi-2nd-order model provided a better fit than the quasi-1st-order model, corresponding to a higher R^2 (0.9821), which is consistent with the $Q_{e,exp}$.

As shown in Fig. 6, the adsorption of AFB$_1$ by DC/CFOS NC occurred at different rates in three steps (boundary layer diffusion, intra-particle diffusion, and gradual sorption). At 0.0–80 min, the rapid enhancement in adsorption capacity (and removal efficiency) of DC/CFOS NC to 3.441 mg g^{-1} (and 91.40%) was due to the existence of sufficient amounts of accessible vacant adsorption sites for AFB$_1$. The experimental results demonstrated that the adsorption process may begin from the outer surface of DC/CFOS NC through boundary layer mass transfer. At the intra-particle diffusion step (80–100 min), the adsorption performance was enhanced with a very gentle slope, and eventually leveled off with the extension of the adsorption time (>100 min). In the third step, the outer surface of DC/CFOS NC was saturated, and thereby the adsorbed-AFB$_1$ diffused in DC/CFOS NC to construct a complex. Thus, the best adsorption time for the whole adsorption of AFB$_1$ from solution is 100 min through the interplay of boundary layer diffusion and/or intra-particle diffusion. Besides, the Weber–Moris intra-particle diffusion model (eqn (18)) proved that the adsorption rate was largely dominated by the boundary layer diffusion step

Table 1 Physicochemical properties and adsorptive detoxification efficiency of the various samples for the removal of AFB$_1$

Sample	D_{ads}[a] (%)	S_{BET}[b] (m^2 g^{-1})	MPD (nm)
C/CFOS	~53.50	17.50	12.70
DC/CFOS	93.10	23.22	15.45
Acid-treated DC/CFOS	80.12	21.45	14.20

[a] Reaction condition: [AFB$_1$]$_0$ = 50.0 μg mL^{-1}, [DC/CFOS]$_0$ = 2.50 mg L^{-1}, pH = 7.0, contact time = 100 min, and temperature = 25 °C. [b] BET surface area.

Table 2 The fitting parameters and correlation coefficient of various adsorption kinetic models[a]

	Quasi-1st-order ($Q_t = Q_e - Q_e e^{K_1 t}$)			Quasi-2nd-order $\left(Q_t = \dfrac{K_2 Q_e^2 t}{1 + K_2 + Q_e t}\right)$			Intra-particle model ($Q_t = k_i(t^{1/2}) + C$)		
Absorbent	Q_e (mg g^{-1})	k_1 (min^{-1})	R^2	Q_e (mg g^{-1})	k_2 (g mg^{-1} min^{-1})	R^2	k_i (mg g^{-1} min^{-5})	C (mg g^{-1})	R^2
DC/CFOS	4.567	−0.313	0.966	34.48	0.199	0.9821	0.184	0.659	0.872

[a] Reaction condition: [AFB$_1$]$_0$ = 50.0 μg mL^{-1}, [DC/CFOS]$_0$ = 2.50 mg L^{-1}, pH = 7.0, contact time = 100 min, and temperature = 25 °C.

because of the lower slope of the intra-particle diffusion step compared with the boundary layer diffusion step (see Fig. 6F).[13,30–34]

$$Q_t = k_i (t_{1/2}) + C \qquad (18)$$

where Q_t is the adsorption capacity at a specific time (mg g^{-1}), k_i is the intra-particle diffusion rate constant (g mg^{-1} min^{-1}), C is the surface adsorption, and t is time (min).

3.3.5. Adsorption isotherm. Fig. 7A exhibits that the adsorption capacity (and removal efficiency) was dramatically enhanced from ∼123.20 μg g^{-1} (39.40%) to 169.22 μg g^{-1} (97.40%) with an increase in the ambient temperature from 5.0 °C to 25 °C. Nevertheless, as the temperature further increased to 35 °C there was a slight decline to 158.2 μg g^{-1} (91.13%). It has been suggested that the molecular mobility of a material increases dramatically when the temperature increases from 5.0 °C to 25 °C, which is due to the increase in

the effective interaction between DC/CFOS NCs and AFB$_1$ molecules; however, higher temperatures resulted in the lower binding affinity of AFB$_1$ to DC/CFOS NC. Besides, the adsorption capacity of AFB$_1$ at 278 K, 288 K, 298 K, and 308 K was 1.785 mg g^{-1}, 2.657 mg g^{-1}, 3.891 mg g^{-1}, and 3.427 mg g^{-1}, respectively, revealing an optimal temperature at ambient temperature (25 °C).

Adsorption isotherm data are indispensable to explain the surface properties of an adsorbent, where the saturated adsorption capacity of the adsorbent, the relationship between the saturated adsorption capacity and the equilibrium concentration, and mechanism at constant temperature can be described by different theoretical adsorption models (e.g., Langmuir, Freundlich, Temkin, Dubinin–Radushkevich). The Langmuir and Freundlich isotherm models describe the mechanistic path of the adsorption process on an absorbent with a homogenous surface (active sites with the same affinity
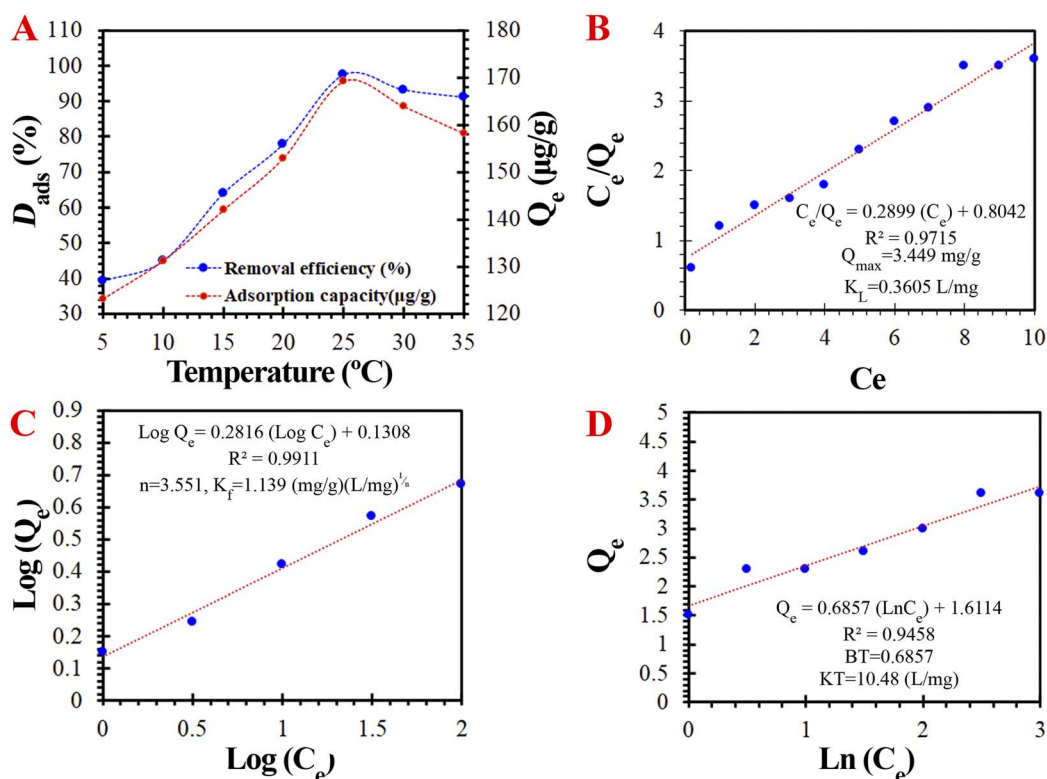

Fig. 7 (A) Adsorption capacity and removal rate of AFB$_1$ at various temperatures [pH 7.0, 120 min] and fitting lines of (B) Langmuir model, (C) Freundlich model, and (D) Temkin model.

Table 3 The fitting parameters and correlation coefficient of the various isotherm adsorption models[a]

Temperature (K)	Freundlich isotherm			Langmuir isotherm				Temkin isotherm		
	R^2	K_f (mg g^{-1}) (L mg^{-1})	n	R^2	R_L	Q_{max} (mg g^{-1})	K_L (L mg^{-1})	R^2	BT	K_t (L mg^{-1})
278	0.934	0.774	3.663	0.881	—	1.781	0.163	0.883	0.561	8.011
288	0.976	0.885	3.991	0.952	—	2.749	0.250	0.913	0.702	9.150
298	0.991	1.139	3.551	0.972	0.399	3.449	0.360	0.959	0.686	10.48
308	0.987	1.067	4.012	0.979	—	3.427	0.295	0.962	0.740	8.125

[a] Reaction condition: $[AFB_1]_0 = 50.0$ µg mL^{-1}, $[DC/CFOS]_0 = 2.50$ mg L^{-1}, pH = 7.0, contact time = 100 min, and temperature = 25 °C.

and monolayer adsorption theory) and heterogeneous surface (actives site with different affinity and multilayer adsorption theory), respectively. Based on the Langmuir model (eqn (5)), the intramolecular interactions are reduced as the interspace of the adsorbent surface and AFB_1 increase and each AFB_1 molecule is absorbed only on a single active binding center. To obtain insight into the adsorption status of DC/CFOS NC and the dominant mechanism of the adsorption process, the trend curve of the equilibrium adsorption amount of DC/CFOS NC for AFB_1 was utilized. Fig. 7 exhibits the nonlinear fitting isothermal adsorption models and the corresponding parameters and correlation coefficient (R^2) are listed in Table 3.

The degree of fitting for the Freundlich model is much higher than other models based on their high R^2 values (Freundlich (0.9911), Langmuir (0.9715), and Temkin model (0.9458)). Thus, the adsorption process proceeds by multilayer adsorption on the heterogeneous surface of DC/CFOS NC with powerful adsorptive interactions between DC/CFOS NC and AFB_1 molecules ($n > 1$, eqn (6)).[13,30,34]

3.3.6. Adsorption thermodynamics. Thermodynamic mechanism studies, which reflect the spontaneity and absorbed/released heat property of AFB_1 adsorbed on DC/CFOS NC, were performed at various temperatures (288, 298, and 308 K) with the initial dosage of 50.0 µg mL^{-1} AFB_1. As is known, a large $|\Delta G°|$ with an increase in temperature can mean a stronger adsorption driving force (spontaneity) and *vice versa*. In addition, an increase in the adsorption temperature led to a decrease in adsorption capacity, demonstrating that the lower temperature contributed to the adsorption process. The negative values of ΔG^0 at various temperatures proved that the solid–liquid adsorption process occurred spontaneously and the affinity between DC/CFOS NCs and AFB_1 was high (Table 4). Furthermore, the negative values of ΔH and positive value of ΔS (calculated from the slope and intercept of the plots of Ln $K°$ *vs.* $1/T$) demonstrate the exothermic character of the process and

the presence of a solid–liquid interface between DC/CFOS NC and AFB_1. The positive value of $\Delta S°$ for the adsorption of AFB_1 proved an enhancement in the randomness at the solid–liquid interface and hydrophobic interaction may exist between DC/CFOS NC and AFB_1. These results proved that higher temperature was a relatively unfavorable condition for the adsorption of AFB_1. Furthermore, the polar noncovalent interactions between the available –OH, –NH$_2$, C=N, and dopamine moieties of DC/CFOS NC and two C=O groups of the AFB_1 molecule are the dominant driving force. Thus, based on the kinetics and thermodynamic studies, both physical adsorption (*e.g.*, pore filling) and chemisorption (*e.g.*, hydrogen bonding and electrostatic interactions) occurred during the adsorption of AFB_1 on DC/CFOS NC. Also, considering that high temperature may cause high energy consumption, and also the loss of nutrients in food, the adsorption of AFB_1 in contaminated samples was subsequently studied at 298 K.

3.4. Adsorption mechanisms

The pathway for the adsorption process consists of two stages, including (i) the fast diffusion of AFB_1 molecules from solution to the delicate solvent layer on the DC/CFOS NC surface and (ii) the slow diffusion of AFB_1 molecules to the surface of DC/CFOS NC, accompanied by pore and layer diffusion, and subsequently an increase in chemical/physical interactions to form the stable complex of [AFB_1—DC/CFOS]. The dopamine modification increased the adsorption capacity by increasing the hydrophobicity and the affinity of the adsorbent to AFB_1. The FT-IR spectrum of the spent DC/CFOS NC illustrated that the peaks corresponding to the hydroxyl, amine, and imine groups slightly shifted from 3684, 3442, and 1647 cm^{-1} to a lower wavenumber of 3673, 3434, and 1632 cm^{-1}, respectively, due to the diminished density of electrons in the spent DC/CFOS NC compared to the fresh DC/CFOS. Besides, the change in the intensity of the peaks in the range of 2853–2963 cm^{-1} and 1585 cm^{-1} corresponding to the C–H and C=O groups, respectively, confirm the chemical interactions between the AFB_1 molecules and alkane chain and carbonyl groups of the adsorbent. These data and kinetic studies (Fig. 6) illustrate that the solid–liquid adsorption process was mainly controlled by the synthetic results of surface complexation and chemical adsorption through the chemical binding of two C=O and dihydrofuran moieties of AFB_1 and the –OH, –NH$_2$, and dopamine moieties on the surface of DC/CFOS NCs. The adsorptive

Table 4 The adsorption thermodynamic parameters for AFB_1 adsorbed on DC/CFOS NC

Temperature (K)	ΔG^0 (kJ mol^{-1})	ΔH^0 (kJ mol^{-1})	ΔS^0 (J mol^{-1} k^{-1})
288	−3.245	—	—
298	−3.147	−2.001	10.11
308	−3.851	—	—

Fig. 9   (A) Run number plot *vs.* residual, (B) normal probability plot of externally studentized residual, (C) plots of predicted responses *vs.* actual experimental values for removal of AFB$_1$ using DC/COFS NC, (D) D_{ads} *vs.* catalyst concentration, and (E and F) RSM optimization response (two-factor graph).

removal imply the high degree of precision and reliability for the model analysis.[29] Besides, the curved nature of the 3D response surface and 2D contour plots prove the mutual interactions between the independent variables with *p*-value < 0.05.[29,36] According to the results, the pH parameter was identified as a non-influential parameter due to its low *F*-value (0.07), followed by temperature (0.14), time (23.12), [AFB$_1$]$_0$ (27.43), and [DC/CFOS]$_0$ (57.19). The RSM measured the removal efficiency of AFB$_1$ under the predicted optimum conditions ([D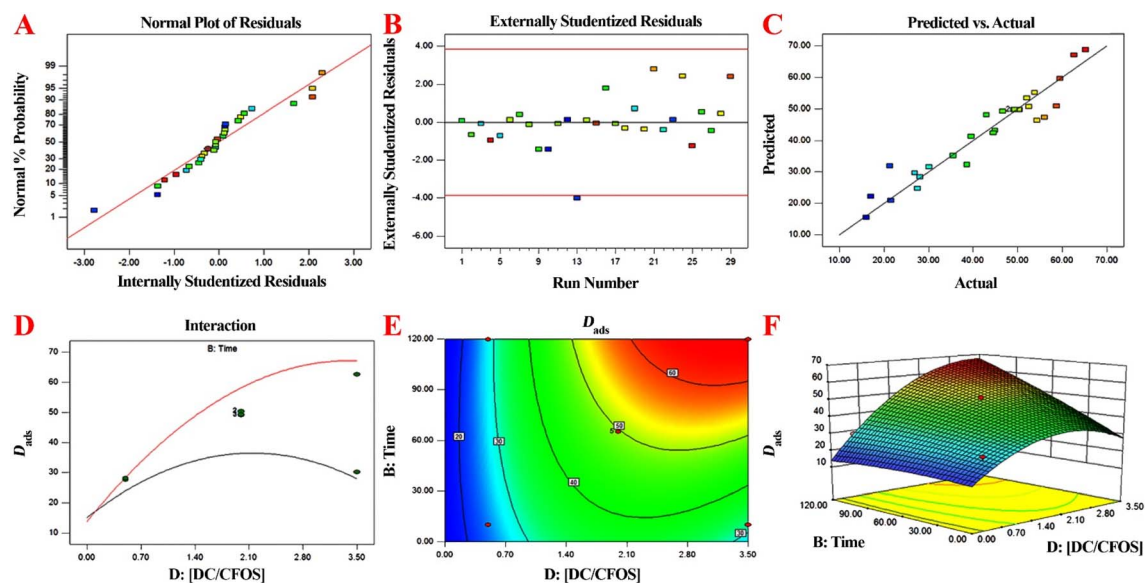C/CFOS] = 3.092 mg L^{-1}, [AFB$_1$] = 51.89 µg mL^{-1}, [temperature] = 26.37 °C, [time] = 108.94 min, and [pH] = 6.97), which was 90.561%, with the desirability of 0.957, as demonstrated by the following experimental results (90.25%, 91.03%, 89.80% and 90.10%) under the predicted optimum conditions. A further increment in [DC/CFOS]$_0$ and time over the optimum value resulted in a decrease in the AFB$_1$ removal efficiency, which is mainly due to the aggregation of DC/CFOS NC. Finally, the comparison of the experimental results with the predicted values showed a high correlation.

3.6.   Quality analysis of the treated edible oil

The adsorption process inevitably leads to a change in some quality factors in oil matrices. Considering the national standard limit required for edible oil (2.0 µg kg^{-1}) in EC, the initial AFB$_1$ content was selected as 2.50 µg kg^{-1} in the following experiments. Alternatively, with an increase in temperature (5.0–25 °C), the viscosity of edible oil declined, and subsequently improved the rate of mass transfer, enhancing the adsorption performance from ~45.6% to ~92.13%. Typically, at a higher temperature, the possible side reactions (*e.g.*, oxidation, hydrolysis, polymerization, and isomerization) of the nutritious components and increasing POV may be caused by the reduction in the quality of the edible oil. Alternatively, an increase in the temperature in the range of

25 °C to 50 °C caused a slight decrease in the adsorption efficiency (~6.00% based on the weight of edible oil) and increasing POV, which proved that the reaction temperature had an negligible influence on the adsorption performance of DC/CFOS NC in the edible oil matrices. The spiked edible oil samples were incubated for 2 h, and then the AFB$_1$ content was measured by UV-Vis spectroscopy at λ_{max} 364 nm. The experimental data proved that DC/CFOS NC successfully adsorbed the AFB$_1$ molecules (~92.13%) from the edible oil matrices. The decrease in adsorption efficiency in oil compared to water is mainly due to the presence of saturated/unsaturated fatty acids such as linoleic acid (C18 : 2 *cis*), oleic acid (C18 : 1 *cis*), and palmitic acid (C16 : 0), which can bind to the interlayers and surface of DC/CFOS NC, subsequently deactivating the active sites for the adsorption of the AFB$_1$ molecules (Fig. 5S†). Besides, the impact of the adsorption process on the physicochemical quality factors of edible oil was assessed during a removal time in the range of 0–120 min. The CFOS NP contents in the samples (prepared by microwave-assisted HCl/HNO$_3$ digestion) were determined by ICP-OES analysis. The results confirmed that Fe and Co were not released in the edible oil, which demonstrated that DC/CFOS NC had excellent durability/stability during the removal process. Furthermore, the data demonstrated that the physicochemical quality factors (*e.g.*, IV, MV, and FFA) of the adsorptive-treated edible oil had no significant change during the solid–liquid adsorption process (P ≥ 0.05), confirming the advantages of DC/CFOS compared to the previously reported removal systems.[37,38] AV, POV, and *p*-AV, corresponding to the oxidative rancidity of the adsorptive-treated edible oil, exhibited a remarkable enhancement (P < 0.05) with a long treatment time (>300 min). The experimental data confirmed that the AV and POV of the treated edible oil ranged from 0.3491 ± 0.006 to 0.3830 ± 0.004 mg g^{-1} and 0.040 ± 0.005 to 0.045 ± 0.007 g per 100 g oil at 120 min, respectively. However,

both the AV and POV of the adsorptive-treated edible oil were still lower than the national standard for AV (≤ 0.5 mg g^{-1}) and POV (≤ 0.25 per 100 g). These observations confirmed that the overall quality of the edible oil after the adsorption of AFB$_1$ using DC/CFOS NC had little change compared to the untreated edible oil. The IV and MV of adsorptive-treated edible oil had no significant change ($P \geq 0.05$) along with the storage period (Table 5). As mentioned, there was no conspicuous change in the composition of the UFAs (18 : 1, 18 : 2, 18 : 3, and 20 : 1), SFAs (16 : 0, 18 : 0, 20 : 0, 22 : 0 and 24 : 0), and sterols in the edible oil sample, demonstrating that the fatty acid profile in the treated edible oil was similar and relatively stable ($P \geq 0.05$). Also, the increase in the AV, POV, and p-AV values in the treated edible oil ($P < 0.05$) during the storage time demonstrate that these phenomena were related to the change in the original edible oil, which was still below the national standard value for AV (≤ 0.5 mg g^{-1}) and POV (≤ 0.25 per 100 g). Besides, no metals were detected in the treated samples, indicating the durability, and also effective magnetic separation of the adsorbent from the reaction medium. Consequently, it can be stated that a large quantity of secondary oxidation by-products (such as ketones and aldehydes) was produced during the adsorption/storage process in the treated edible oil matrices, but the overall quality of the treated edible oil was still satisfactory after adsorption/storage period.

3.7. Recycling and regeneration of the adsorbent

The recovery results illustrated that DC/CFOS has excellent reproducibility and recoverability, achieving 81.30% and

72.20% removal efficiency after 6 recycling cycles of removing AFB$_1$ from water and edible oil, respectively (Table 6). Besides, the desorption (%) by HCl was more favorable than desorption by NaOH in all the adsorption–desorption runs. In the first and sixth desorption runs, the HCl desorption solution resulted in ~93.50% and 72.20% AFB$_1$ desorption from DC/CFOS NC, while the NaOH desorption solution achieved ~52.50% and 18.5% AFB$_1$ desorption, respectively. Thus, it seems that HCl can protonate the surface of DC/CFOS NC.[39,40]

3.8. Comparison with existing absorbents for the removal of AFB$_1$

The development of the innovative application of efficient sorbents for the removal of AFB$_1$ is essential. Many important parameters are considered in the design of effective adsorbents for the removal of AFB$_1$ such as maximum adsorption capacity/removal efficiency, simple fabrication, large volume of small pores, mild reaction conditions, low cost, and reusability. Therefore, the adsorption capacity of DC/CFOS NC and other adsorbents for AFB$_1$ in water and/or food samples is presented in Table 3S.† The comparison of the data proved that DC/CFOS NC is capable of attaining similar or even better reaction conditions (*e.g.*, short time, ambient temperature, relatively lower dose, wide pH range, and without the need for additives), maximum adsorption performance, and applicability in food samples without the feasible destruction of food nutrients. Compared to non-magnetic adsorbents, DC/CFOS NC can be easily isolated by an external magnet field, proving the utility and practicality of the synthesized porous nanocomposites. Thus, DC/CFOS NC is superior for removing AFB$_1$ from aqueous and non-aqueous matrices (Table 3S†).

3.9. Adsorption efficiency for mixed mycotoxin solution

The similar concentration of a solution of various mycotoxins (*i.e.*, AFB$_1$ (aflatoxin B1), AFB$_2$ (aflatoxin B2), FB1 (fumonisin B1), ZEN (zearalenone), and DON (deoxynivalenol)) was mixed and their adsorptive removal evaluated. The results indicated that the D_{ads} for the adsorption of various mycotoxins followed the order of AFB$_1$ (93.10% ± 1.1%) > AFB$_2$ (86.20% ± 2.5%) > ZEN (80.30% ± 2.7%) > DON (50.50% ± 3.4%) > and FB1 (21.60% ± 4.8%). Based on eqn (15) and (20), the selectivity coefficient (a) was determined.[41]

$$a = \frac{K_{d1}}{K_{d2}} \quad (20)$$

Table 5 The quality change in treated corn oil during the degradation process and storage

Quality factor	Oil samples^a		
	Control^b ($t = 0$)	Treated oil	Stored oil
AV (mg g^{-1})	0.3491 ± 0.35	0.3830 ± 0.54	0.3835 ± 0.56
IV (g per 100 g)	130.00 ± 2.40	135.0 ± 2.78	134.0 ± 3.56
POV (g per 100 g)	0.040 ± 0.31	0.045 ± 0.44	0.0401 ± 0.82
p-AV (g per 100 g)	3.6 ± 0.12	3.66 ± 0.10	4.02 ± 0.15
MV	0.0 ± 0.01	0.0	0.0
RI	1.47 ± 0.092	1.47 ± 0.65	1.47 ± 0.080
D	1.471 ± 0.067	1.471 ± 0.094	1.472 ± 0.054
TV	11.60 ± 0.13	11.66 ± 0.14	12.02 ± 0.84
Ac	6.95 ± 0.03	7.62 ± 0.05	7.81 ± 0.09

^{a} Condition reaction: temperature = 25 °C, contact time = 100 min, [AFB$_1$]$_0$ = 50.0 µg mL^{-1}, and [DC/CFOS]$_0$ = 2.50 mg L^{-1}. ^{b} Values are means ± SD ($n = 3$).

Table 6 Reusability of DC/CFOS for the removal of AFB$_1$ from water

Cycle^a	Fresh	1	2	3	4	5	6
D_{ads} (%)	97.40	91.00	91.20	90.34	90.20	90.10	81.30
Desorption (%)^b	96.45	94.70	93.10	91.00	89.45	87.60	72.20
Q_{max} (mg g^{-1})	3.449	3.448	3.448	3.447	3.236	3.126	3.010
Residue concentration (mg L^{-1})	1.280	1.370	2.340	2.560	7.500	9.560	11.50

^{a} Condition reaction: temperature (25 °C), time (100 min), [AFB$_1$]$_0$ (50.0 µg mL^{-1}), and [DC/CFOS]$_0$ (2.50 mg L^{-1}). ^{b} (H$_2$O/CH$_3$CN 85/15 v/v).

where, K_{d1} and K_{d2} represent the distribution coefficient of AFB_1 and competitive mycotoxin, respectively. The selectivity coefficients for AFB_1/AFB_2, AFB_1/ZEN, AFB_1/DON, and $AFB_1/FB1$ were 1.08, 1.17, 1.86, and 4.11, respectively, indicating the relatively low selectivity of DC/CFOS NC. This difference in efficiency can be related to various reasons, as follows: (i) the polar nature and molecular mass of the toxins, (ii) the presence of π–π interactions between the benzene ring of the adsorbent and some target toxins, (iii) the relative strength of H-bonding between the amino/hydroxyl groups of the adsorbent and mycotoxins.

4. Conclusion

In summary, we fabricated DC/CFOS NC as a superior adsorbent for the temperature/pH-dependent adsorption of AFB_1 from aqueous and organic phases. After embedding dopamine/amine groups in chitosan cobalt ferrite nanoparticles, the highest adsorption performance was observed compared to the soluble/insoluble unmodified chitosan due to the size, nanodomain, and porous structure of the adsorbent, the synergistic effect between the surface area and the amount of hydrophobic chains and hydrophilic moieties, high structural/chemical stability, and magnetically recoverability of the DC/CFOS nanocomposite. The adsorption capacities of DC/CFOS NC for AFB_1 in water, edible oil, and corn oil were 3.449, 3.127, and 3.106 mg mg^{-1}, respectively, which are relatively higher than that of other reported adsorbents. Multiple chemical/physical adsorption mechanisms, including π–π stacking, complexation, and hydrophobic interactions, controlled the adsorption process. Besides, DC/CFOS NC had little impact on the quality factors of edible oil and corn oil, which proved the safety of the adsorptive process for the removal of AFB_1 from oils using DC/CFOS NC.

Conflicts of interest

No conflict to declare.

Acknowledgements

References

1 Q. Du, W. Zhang, N. Xu, X. Jiang, J. Cheng, R. Wang and P. Wang, *Food Chem.*, 2023, **418**, 135881.

2 A. R. Faraji, N. B. Khoramdareh, F. Falahati, S. Jafari, S. A. Monfared and A. Faghih, *Int. J. Biol. Macromol.*, 2023, **234**, 123709.

3 D. Gizachew, C. H. Chang, B. Szonyi, S. De La Torre and W. T. E. Ting, *Int. J. Food Microbiol.*, 2019, **296**, 8–13.

4 S. Sun, R. Zhao, Y. Xie and Y. Liu, *Food Chem.*, 2021, **343**, 128521.

5 X. Wang and W. Jia, *J. Hazard. Mater.*, 2023, **458**, 132021.

6 Z. Ying, T. Zhang, H. Li and X. Liu, *Food Chem.*, 2023, **409**, 135321.

7 P. Li, S. Wang, B. Lv, M. Zhang, C. Xing, X. Sun and Y. Fang, *Food Control*, 2023, **152**, 109883.

8 B. Van de Voorde, B. Bueken, J. Denayer and D. De Vos, *Chem. Soc. Rev.*, 2014, **43**, 5766–5788.

9 J. Ji and W. Xie, *Food Chem.*, 2021, **339**, 128072.

10 F. Meng, W. Ma, C. Duan, X. Liu, Z. Chen, M. Wang, J. Gao and Z. Zhang, *Appl. Catal., B*, 2019, **252**, 187–197.

11 A. Delgado-Cedeño, S. P. Hernández-Martínez, Y. Ramos-Zayas, A. G. Marroquín-Cardona, G. Méndez-Zamora, M. A. Franco-Molina and J. R. Kawas, *Front. Mater. Sci.*, 2022, **9**, 1044495.

12 S. Sid, R. S. Mor, A. Kishore and V. S. Sharanagat, *Trends Food Sci. Technol.*, 2021, **115**, 87–104.

13 Y. Li, G. Tian, B. Chen and J. Liang, *Sep. Purif. Technol.*, 2022, **291**, 120953.

14 Y. Luo, X. Liu, L. Yuan and J. Li, *Trends Food Sci. Technol.*, 2020, **96**, 127–134.

15 M. de Jesús Nava-Ramírez, A. M. Salazar, M. Sordo, C. López-Coello, G. Téllez- Isaías, A. Méndez-Albores and A. Vázquez-Durán, *Food Chem.*, 2021, **345**, 128863.

16 T. Lu, C. Fu, Y. Xiong, Z. Zeng, Y. Fan, X. Dai, X. Huang, J. Ge and X. Li, *J. Agric. Food Chem.*, 2023, **71**, 3876–3884.

17 M. Keshvardoostchokami, M. Majidi, A. Zamani and B. Liu, *Carbohydr. Polym.*, 2021, **273**, 118625.

18 P. Arévalo-Cid, J. Isasi and F. Martín-Hernández, *J. Alloys Compd.*, 2018, **766**, 609–618.

19 Z. Mahhouti, H. El Moussaoui, T. Mahfoud, M. Hamedoun, M. El Marssi, A. Lahmar, A. El Kenz and A. Benyoussef, *J. Mater. Sci.*, 2019, **30**, 14913–14922.

20 F. M. Reicha, A. Sarhan, M. I. Abdel-Hamid and I. M. El-Sherbiny, *Carbohydr. Polym.*, 2012, **89**, 236–244.

21 L. Qi, Z. Xu, X. Jiang, C. Hu and X. Zou, *Carbohydr. Res.*, 2004, **339**, 2693–2700.

22 S. Slimani, A. Talone, M. Abdolrahimi, P. Imperatori, G. Barucca, D. Fiorani and D. Peddis, *J. Phys. Chem. C*, 2023, **127**, 8840–8849.

23 A. R. Faraji, F. Ashouri, Z. Hekmatian, S. Heydari and S. Mosazadeh, *Polyhedron*, 2019, **157**, 90–106.

24 M. A. Nasseri, K. Hemmat, A. Allahresani and E. Hamidi-Hajiabadi, *Appl. Organomet. Chem.*, 2019, **33**, 4809.

25 T. Lei, X. Jiang, Y. Zhou, H. Chen, H. Bai, S. Wang and X. Yang, *J. Colloid Interface Sci.*, 2023, **636**, 153–166.

26 F. Chen, S. Xie, X. Huang and X. Qiu, *J. Hazard. Mater.*, 2017, **322**, 152–162.

27 S. Menchaca-Nal, J. A. Jativa-Herrera, O. Moscoso-Londoño, L. G. Pampillo, R. Martínez-García, M. Knobel and C. L. Londoño-Calderón, *Mater. Chem. Phys.*, 2023, **303**, 127798.

28 F. Ma, P. Li, B. Zhang and Z. Wang, *Int. J. Biol. Macromol.*, 2017, **103**, 501–507.

29 A. R. Faraji, N. B. Khoramdareh, S. Ahmadi, A. Gil, A. Farahanipour and Z. Hekmatian, *J. Environ. Chem. Eng.*, 2023, **11**, 109668.

30 N. Zhang, N. Li, X. Han, H. Zhang, J. Meng, P. Zhou and J. Liang, *J. Alloys Compd.*, 2023, **960**, 170800.

31 Y. Wang, C. Hou, Y. Dai, L. Chu, S. Geng, S. Zheng and X. Kang, *Anal. Methods*, 2023, **15**, 472–481.

32 D. Roy, B. Roy and A. K. Manna, *Groundw. Sustain. Dev.*, 2023, 101020.

33 Y. Zhou, R. Wang, Z. Chen, X. Luo, L. Wang, X. Zhao, C. Zhang and P. Yu, *Food Chem.*, 2022, **389**, 132987.

34 F. Ma, Q. Guo, Z. Zhang, X. Ding, L. Zhang, P. Li and L. Yu, *Food Chem.*, 2023, **428**, 136779.

35 E. O. Pérez-Gómez, G. García-Rosales, L. C. Longoria-Gándara and J. C. Gómez-Vilchis, *J. Hazard. Mater.*, 2022, **424**, 127339.

36 S. Movahedian, A. R. Faraji and F. Ashouri, *New J. Chem.*, 2023, **47**, 2329–2342.

37 S. F. Wong, A. N. T. Tiong and Y. H. Chin, *Biofuels*, 2023, 967–977.

38 J. Wei, X. Wu, C. Wu, F. Hou, L. Wu and H. Huang, *Food Chem.*, 2022, **378**, 132037.

39 E. Asgari, A. Sheikhmohammadi and J. Yeganeh, *Int. J. Biol. Macromol.*, 2020, **164**, 694–706.

40 M. A. P. Cechinel and A. A. U. de Souza, *J. Cleaner Prod.*, 2014, **65**, 342–349.

41 F. Meng, W. Ma, L. Wu, H. Hao, L. Xin, Z. Chen and M. Wang, *J. Taiwan Inst. Chem. Eng.*, 2018, **83**, 192–203.